IEEE Photonics Journal
An IEEE Photonics Society Publication

Open Access

Recovery of Absorption Line Shapes With Correction for the Wavelength Modulation Characteristics of DFB Lasers

Volume 8, Number 3, June 2016

Thomas Benoy, Member, IEEE
Michael Lengden
George Stewart, *Member, OSA*
Walter Johnstone

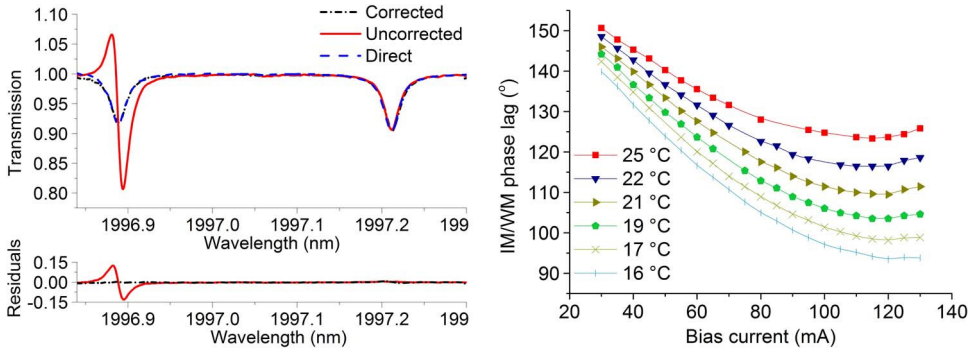

DOI: 10.1109/JPHOT.2016.2558504
1943-0655 © 2016 IEEE

IEEE photonics SOCIETY

IEEE

Recovery of Absorption Line Shapes With Correction for the Wavelength Modulation Characteristics of DFB Lasers

Thomas Benoy, *Member, IEEE*, Michael Lengden, George Stewart, *Member, OSA*, and Walter Johnstone

Centre for Microsystems and Photonics, Department of Electronic and Electrical Engineering, University of Strathclyde, Glasgow G1 1XW, U.K.

DOI: 10.1109/JPHOT.2016.2558504

Manuscript received April 18, 2016; accepted April 20, 2016. Date of publication May 4, 2016; date of current version May 12, 2016. This work was supported by the Engineering and Physical Sciences Research Council under Grant EP/J002178/1. Corresponding Author: M. Lengden (e-mail: michael.legnden@strath.ac.uk).

Abstract: Tunable diode laser spectroscopy combined with wavelength modulation spectroscopy (WMS) is an important technique for noninvasive measurements of gas parameters such as pressure, concentration, and temperature in high-noise harsh environments. A variety of laser types are used for these applications, and the modulation characteristics can have significant effects on line shape recovery. Here, we identify important characteristics of distributed feedback (DFB) lasers that need to be taken into account in the context of WMS and illustrate the effects with a 2-μm wavelength multiquantum-well DFB laser used for CO_2 detection. The modulation response of the laser is measured, and we demonstrate how the phasor decomposition method (PDM) may be used to obtain accurate line shapes from the first harmonic WMS signals by correcting for phase variation across the laser's low-frequency current sweep. We also demonstrate how the PDM approach can be improved by removing the need to preset the orientation of the lock-in axis to isolate the residual amplitude modulation component, making it more suitable for field applications.

Index Terms: Absorption line shape recovery, diode laser spectroscopy, laser modulation, optical gas sensors, wavelength modulation spectroscopy (WMS).

1. Introduction

Tunable diode laser spectroscopy (TDLS) is a powerful tool for the measurement of gas parameters such as concentration, pressure, and temperature in a wide variety of environments [1]–[8]. In the simplest case of direct TDLS, the laser wavelength is scanned across an absorption feature, by applying a saw-tooth current ramp to the diode, and the obtained signal is normalized with a no-gas signal or a non-absorbing baseline to provide an absorption line shape. The gas properties are then calculated using a least square fit of the experimental absorption line shape to a physical spectroscopic line shape model. It is not possible to obtain all three unknowns, i.e., concentration, temperature and pressure, from the least-squares fitting algorithm, as there are only two variables, line shape depth, and width. Therefore, either one of the three gas parameters must be known in advance or another methodology used. For example, ratio thermometry [1] uses the ratio of the peaks of two absorption lines with different lower state energies, or the ratio of their integrated areas, to determine temperature.

Although direct spectroscopy is a simple process, it has limitations in harsh environments, such as measurements of aero engine exhaust plumes [8], where extraneous noise often completely obscures the absorption feature. In this case, phase sensitive detection techniques, such as wavelength modulation spectroscopy (WMS), are commonly used. In WMS an additional high frequency sinusoidal current modulation is applied to the laser producing an intensity modulation (IM) and a time delayed wavelength modulation (WM). The detected signal is fed into a lock-in-amplifier, which then outputs a selected harmonic signal arising from the interaction of the IM and WM with the gas absorption line shape function.

Extensive theoretical analysis of the harmonic signals generated in WMS has been reported over many years [2], [9]–[16]. Our own recent work has focused on separating the IM and WM components at the first harmonic, allowing calibration-free recovery of absolute absorption line shapes, using a no-gas background or a non-absorbing baseline for normalization that is proportional to the IM output from the laser [3], [4], [17]–[21]. Fluctuations in optical transmission can make it difficult to normalize the line shape, due to the variation of IM between the gas and no-gas measurements. Fernholz *et al.* [9] proposed a digital fast scanning WMS detection technique by which the fast intensity fluctuations could be cancelled by averaging a high frequency current scan (1 kHz) and a higher frequency modulation of 300 kHz, followed by demodulation. The cancellation of the low frequency intensity fluctuations is achieved by dividing the second harmonic signal with the first harmonic signal. This method was further developed by Rieker *et al.* [2].

The harmonic signals discussed above depend critically on the absolute magnitudes of the intensity and wavelength modulation produced at the DFB laser source and their relative magnitude and phase, often described in the literature as the Chirp-to-Power Ratio (CPR). In turn, the CPR depends on the electronic, optical, and thermal characteristics of the DFB and is affected by several modulation parameters, including the current modulation amplitude, modulation frequency and the DC bias current. The modulation properties of DFB lasers have been extensively studied in the literature but usually within the context of understanding or reducing the CPR for high performance fiber optic communication networks [22], [23]. For WMS applications, experimental measurement of the magnitude and phase lag of the wavelength modulation as a function of the modulation frequency has been reported for several specific lasers including a 2 μm DFB laser [24], 0.763 – 2.3 μm VCSELs [25] and a 3 μm interband cascade laser [26].

In practice, a wide variety of lasers sources are used for WMS with differing characteristics and it is important not only to choose suitable modulation parameters specific to the source but also to correct the harmonic signals where necessary for variation of these parameters. It is the purpose of this paper to identify the important modulation issues specifically for WMS applications and the effect of the modulation parameters on the implementation of WMS spectroscopy, so as to allow accurate recovery of line shapes and gas parameters from the harmonic signals. Rather than detailed numerical analysis of the modulation characteristics of individual lasers, we use simple analytical models where possible in order to identify the key issues.

We experimentally illustrate the effect of variation in the laser modulation parameters, in particular the walk-off of the WM-IM phase separation across the current scan, for the case of CO_2 detection with a 2 μm quantum well DFB laser. The importance of this phase walk-off correction is highlighted in measurements of two nearby absorption spectral features of CO_2 that can be used for ratio thermometry measurements. The use of a single source for ratio thermometry is advantageous due to the reduction in drive and collection electronics, and the use of two nearby transitions is preferred in ratio-thermometry due to the similar dependence of their spectral parameters on pressure and concentration [1], [2], 5]. However, using a single laser requires a much larger current scan, thus increasing the overall phase walk-off, leading to significant measurement error. It will be shown that the phasor decomposition method (PDM) [18] can be used to recover the two nearby absorption features only if the phase walk-off is accounted for in the line shape recovery signal processing.

We also improve on the PDM technique to render the measurement process independent of the orientation of the lock-in axes. This is of great benefit when WMS detection is combined with optical tomography [8], where multiple measurement paths are used and the alignment of the LIA phase for each path would be overly time-consuming.

2. Modulation Properties of DFB Lasers

Current modulation of DFB lasers gives rise to wavelength modulation as a result of the combination of carrier density modulation and thermal modulation. In this section the contributory carrier density and thermal effects to this wavelength modulation are discussed. Typically, the modulation amplitudes are quoted in the frequency domain and this nomenclature has been adopted in this paper. However, to avoid confusion between WMS and frequency modulation spectroscopy (FMS) the discussion will be in terms of the wavelength modulation (WM) rather than the frequency modulation (FM), where these two effects differ in phase by 180°.

2.1. Carrier Density Modulation

Carrier density modulation results in modulation of the refractive index and hence the output laser wavelength. Several factors are responsible for the carrier density modulation including relaxation oscillation, spectral and spatial hole-burning and the coupling of spontaneous emission to the lasing mode [22], [27]–[34]. Relaxation oscillation effects only become significant near the relaxation oscillation frequency which is normally much higher than the typical frequencies used in WMS. Similarly, the contribution from spontaneous emission is only significant near threshold and can usually be neglected for WMS applications. The spectral hole burning contribution is typically independent of modulation frequency, FM magnitude of ~60 MHz/mA, with the wavelength modulation 180° out of phase with the current modulation. Spatial hole burning effects are more complex and may in some cases be dependent on the bias current. Typical hole-burning effects produce a FM magnitude of ~20–40 MHz/mA.

2.2. Thermal Modulation

Because of the relatively low frequencies employed, thermal modulation plays a very important role in most WMS systems. The temperature modulation within a laser diode can be numerically computed from the heat conduction equation and detailed studies have been performed by a number of authors [35]–[43]. However, to elucidate important features for WMS, we outline the commonly used analytical RC thermal model in the Appendix, and from this, we can make the following important observations for WMS.

1) As a consequence of joule heating in the chip, we note from equations (A.5) and (A.8) that the magnitude of the thermal contribution to the wavelength modulation increases with bias current and, hence, will increase across a sawtooth current ramp scanning the wavelength through the absorption line. In essence, the same magnitude of modulation current produces a greater heat power variation at higher bias current. The significance of this effect depends critically on the magnitude of the laser's ohmic resistance (which can be measured from the *VI* characteristics) and may vary for different lasers. Furthermore, since the thermal contribution is vectorially added to the carrier density contribution, there will be a small change in the resultant phase of the wavelength modulation during a wavelength scan by a sawtooth current ramp.
2) As shown by (A.4) and (A.8) in the Appendix, the wavelength scan from a sawtooth ramp has a nonlinear dependence on applied current (and a small offset determined by the amplitude of the modulation current) as a result of the ohmic resistance.
3) As indicated by (A.6) in the Appendix, there is a small wavelength modulation at the second harmonic of the modulation frequency.

On the basis of the RC model, the magnitude of the thermal response diminishes with increasing frequency, according to a first-order filter response of the form, $(1 + jf_m/f_c)^{-1}$, where f_m is the modulation frequency and f_c is a thermal cut-off frequency and hence the thermal phase lag of the WM with respect to the IM increases from 0° to a maximum of 90°. However, though widely used [28]–[30], a number of authors have noted that this simple model, based on a linear temperature distribution from the active layer to the heat sink, fails to explain certain features observed in the WM response of laser diodes. An inverse square root dependence on modulation frequency and departure from a first order type phase response has been noted for a number of lasers [25], [38], [39], [43]. Also, in order to explain experimentally-observed dips in the WM response, an analytical solution was derived from the heat conduction equation by Dilwali [40] for heat generation in the active layer positioned centrally in a three-layer, 1-D model of a laser chip. However, an average temperature over the whole laser chip is used (rather than an average over the optical mode profile) and the constants have to be arbitrarily adjusted to match the DC response. Hangauer [25] has also derived a semi-analytical thermal model specifically for VCSELs in the form of a Fourier transform equation for numerical integration. In this paper (see Appendix) we derive a 1-D analytical solution of the heat conduction equation based on the assumption of uniform temperature in a thin active layer, which reduces to the RC model at low frequencies but gives a better description of the thermal properties than the RC model. We note the following important differences—see (A.23) in the Appendix. There are two cut-off frequencies associated with the substrate and superstrate layers. At high frequencies, the response has inverse square root behavior of the form: $1/(j\ f_m/f_{cs})^{1/2}$. As a consequence, the WM thermal phase lag approaches 45° rather than 90° and the high frequency roll-off is slower, which concurs with general experimental observations as noted.

2.3. Combined Carrier and Thermal Effects

The total modulation response of DFB lasers results from the phasor combination of the carrier and thermal effects. From the RC model, (A.5) and (A.8) in the Appendix, the magnitude of the optical frequency tuning coefficient (typically in GHz/mA) is

$$\left|\frac{\Delta f}{\Delta i}\right|^2 = \frac{H_0^2 - 2\rho_f H_0}{1 + \left(\frac{\omega_m}{\omega_c}\right)^2} + \rho_f^2. \tag{1}$$

The phase of the frequency modulation relative to the current modulation is $\psi = (\psi_\lambda + \pi)$, where

$$tan\,\psi_\lambda = \frac{\left(\frac{\omega_m}{\omega_c}\right) H_0}{H_0 - \rho_f\left\{1 + \left(\frac{\omega_m}{\omega_c}\right)^2\right\}} \tag{2}$$

and ψ_λ is the phase of the WM relative to the current modulation. Here, ρ_f is the contribution from the carrier density modulation, and is assumed to be constant, independent of the modulation frequency, with its WM in anti-phase with the modulation current.

H_0 is the magnitude of the thermal tuning as $\omega_m \to 0$

$$H_0 = \left(\frac{c}{\lambda^2}\right)\left(\frac{\Delta\lambda}{\Delta T}\right) R_T\{(V_j - \eta) + 2r_s I_{\text{bias}}\}. \tag{3}$$

The various parameters in equation (3) may be determined from measurement of the DC electrical characteristics and from the DC wavelength tuning curve given by

$$\Delta\lambda_{DC} = \left\{\left(\frac{\Delta\lambda}{\Delta T}\right) R_T(V_j - \eta) - \rho_\lambda\right\} I_{\text{bias}} + \left(\frac{\Delta\lambda}{\Delta T}\right) R_T r_s I_{\text{bias}}^2 \tag{4}$$

where $\rho_\lambda = (\lambda^2/c)\rho_f$.

Note from equation (1) that when $H_0 > 2\rho_f$ the magnitude of the tuning coefficient decreases with modulation frequency, whereas when $H_0 < 2\rho_f$ the tuning coefficient actually increases with frequency. For $H_0 = 2\rho_f$ the magnitude of the tuning coefficient is independent of frequency.

For the more advanced thermal model given by (A.23) in the Appendix, the total tuning coefficient (thermal plus carrier) is

$$\frac{\Delta f}{\Delta i} \cong \rho_f - \left\{ \frac{H_0}{\left(\frac{j\omega_m}{\omega_{cs}}\right)^{\frac{1}{2}}\left[\coth\left(\frac{j\omega_m}{\omega_{cs}}\right)^{\frac{1}{2}} + \tanh\left(\frac{j\omega_m}{\omega_{cb}}\right)^{\frac{1}{2}}\right]} \right\} \tag{5}$$

where $\omega_{cs} = \kappa/d_s^2$ and $\omega_{cb} = \kappa/d_b^2$ are the cut-off frequencies associated with the substrate and top layers, respectively, and x is the thermal diffusivity.

Similarly to the RC model above, the magnitude of the tuning coefficient from equation (5) may either decrease or increase with modulation frequency, depending on the relative magnitudes of the thermal and carrier effects. Furthermore, equation (5) also predicts the presence of a dip in the magnitude response for certain laser parameters.

3. Line Shape Recovery With WMS

3.1. Harmonic Signals from WMS

As discussed in Sections 1 and 2, the higher frequency sinusoidal laser drive current modulation in WMS produces an intensity and wavelength modulation at the laser output. The interaction of the IM and WM with an absorption line results in signals at the harmonics of the modulation frequency, whose amplitude and phase depend on the laser modulation characteristics and the absorption line parameters. In general, for lock-in detection of a harmonic at nf, there are three contributions to the signal with magnitude and phase relative to the intensity modulation as follows [20]:

1) a "derivative" component, $-Aa_n I(\nu)$, at phase of $-n\psi$
2) a component, –0.5 $Aa_{n-1}\Delta I(\nu)$, at phase of $-(n-1)\psi$
3) a component, –0.5 $Aa_{n+1}\Delta I(\nu)$, at phase of $-(n+1)\psi$

where a_n are the Fourier coefficients, dependent on the line shape function and the modulation index, $m = \delta\nu/\gamma$, $\delta\nu$ and γ are the frequency modulation amplitude and absorption half-linewidth, ψ is the phase shift between the FM and the IM, A is the gas absorbance at line centre, and $I(\nu)$ and $\Delta I(\nu)$ are the DC laser intensity and intensity modulation amplitude, respectively.

In this work we are primarily concerned with line shape recovery from the first harmonic signal and the three components in this case are

1) $-Aa_1 I(\nu)$, at phase of $-\psi$
2) $-Aa_0\Delta I(\nu)$, at reference phase of zero
3) $-0.5\ Aa_2\Delta I(\nu)$, at phase of -2ψ

plus the background RAM, $\Delta I(\nu)$, at reference phase zero. See (7) and (8) for the first harmonic lock-in signal with these components.

As explained in our earlier work [17]–[21], calibration-free line shape recovery is based on subtracting the derivative component 1) above and using the background RAM to normalize component 2) to yield Aa_0. For small modulation indices, the a_2 component 3) may be neglected, and the line shape is given directly by a_0, but for larger indices, a correction factor is necessary [20]. In this paper, we explain how we can deal with phase changes arising from the

modulation characteristics of the laser source and introduce an additional feature to render the measurement process with the PDM to be independent of the lock-in phase.

3.2. Phasor Decomposition Method

In the PDM, the *x*-axis of the LIA is aligned in-phase with the background RAM and measurements are taken from both the *x*- and *y*-axis. If these two measurements are combined at every point in the scan [20] then the derivative component is eliminated since

$$X_{\text{lock-in}} + \frac{Y_{\text{lock-in}}}{\tan(\psi_\lambda)} = \Delta I(\nu)\{1 - A(a_0 - 0.5a_2)\} \tag{6}$$

which leaves the desired signal after normalization by $\Delta I(\nu)$, or alternatively RAM nulling techniques [44], [45] may be used. Previous application of the PDM assumed ψ_λ to be constant and that it could be calculated from the obtained first harmonic signals. However, as explained in Section 2, this will not be the case if the ohmic resistance of the laser is significant or a large current scan is necessary. In such cases it is necessary to measure ψ_λ either in-situ or prior to carrying out WMS, and apply the varying phase to equation (6).

Unlike other WMS methods, such as $nf/1f$ techniques, which are phase-independent [5], the PDM as described above requires the lock-in phase to be aligned with the RAM component. This can be inconvenient in practical applications, for example when the PDM is used in conjunction with optical tomography where in excess of 126 optical paths are used [8], that all require their lock-in phases to be aligned. However, we can also render the PDM independent of the lock-in phase as follows. For an arbitrary orientation, θ_L, of the lock-in *x*-axis with respect to the RAM, the signals measured on the *x*- and *y*-axis are

$$\begin{aligned} X_{\text{lock-in}} &= \Delta I(\nu)(1 - Aa_0)\cos(\theta_L) \\ &\quad + Aa_1 I(\nu)\cos(\theta_L + \psi_\lambda) \\ &\quad - 0.5Aa_2\Delta I(\nu)\cos(\theta_L + 2\psi_\lambda) \end{aligned} \tag{7}$$

$$\begin{aligned} Y_{\text{lock-in}} &= -\Delta I(\nu)(1 - Aa_0)\sin(\theta_L) \\ &\quad - Aa_1 I(\nu)\sin(\theta_L + \psi_\lambda) \\ &\quad + 0.5Aa_2\Delta I(\nu)\sin(\theta_L + 2\psi_\lambda). \end{aligned} \tag{8}$$

The processing software then computes the combination

$$X_{\text{lock-in}} + \frac{Y_{\text{lock-in}}}{\tan(\theta + \psi_\lambda)} \tag{9}$$

where θ is iterated from 0 to 180° in intervals of 0.2°. The a_1 component will only be completely removed from equation (9) when $\theta = \theta_L$ and this is recognized in the software processing by the least difference between the non-absorbing baseline and the maximum absorption point. At other values of θ, the addition of contributions from the a_0 and a_1 components in equation (9) results in an increased peak height of the measured signal—see [3].

The software iteration time is ~0.4 seconds using a MATLAB code that calculated the PDM outputs for all values of θ in parallel. This process can be optimized for real time applications through improvements to the software coding and the use of a dedicated PC with a high speed processor.

4. DFB Laser Characterization

The optical source used in this work is a DFB laser from Eblana photonics with a multiple quantum well (MQW) gain region and its structure is detailed in reference [46]. It consists of three 8 nm thick quantum wells and four 15 nm thick barriers sandwiched between two 250 nm thick confinement layers, with a top layer of 2 μm thickness and an InP substrate thickness of 120 μm. A 3 μm width ridge of cavity length 600 μm forms the waveguiding

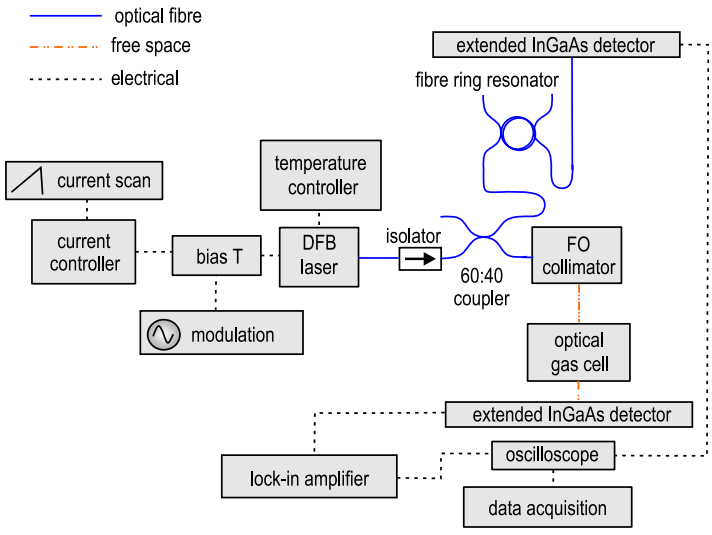

Fig. 1. Experimental measurement system for laser characterization and gas detection.

region. Using these dimensions, the theoretical thermal resistance, calculated from equation (A.9), is $R_T \approx 40$ °C/W and the theoretical thermal cut-off frequencies of the substrate and top layer in the planar model of (5) are 0.5 kHz and 1.8 MHz, respectively. From the measured VI characteristic, the ohmic resistance is $r_s \sim 5\ \Omega$ and the junction voltage is $V_j \sim 0.82$ V and from the *LI* curve the slope efficiency, $\eta \sim 0.046$ W/A. Experimental measurement of the DC tuning characteristics suggested an experimental value of $R_T \approx 50$ °C/W with $\Delta\lambda/\Delta T \cong 0.11$ nm/°C.

4.1. Measurement of the Tuning Coefficient and WM-IM Phase (ψ_λ)

The experimental arrangement for measuring the laser WM-IM phase and tuning coefficient is shown in Fig. 1. The temperature of the laser is controlled by a Thorlabs TED 200 PID temperature controller, and the current is supplied using a Thorlabs LDC 210 and a signal generator via a bias T, used to sum the DC ramp and the high frequency modulation. The output light from the laser passes through a 60:40 fiber coupler, with one output designated as the "measurement arm" and the second output designated as the "wavelength referencing" arm. The measurement arm contains a fiber-coupled collimator with a 2 μm central wavelength, used to direct light through a 5.5 cm long optical gas cell and onto an extended InGaAs photodetector (Thorlabs-PDA 10D-EC). The wavelength referencing arm comprises of a fiber ring resonator, with an FSR of 0.124 GHz, connected to another extended InGaAs detector.

A typical fiber ring resonator trace, and corresponding IM signal from the measurement arm, is shown in Fig. 2 for a modulation frequency of 200 kHz and current modulation amplitude of 10 mA, where the gas cell in the measurement path is filled with nitrogen. The oscilloscope sampling rate is 100 MS/s, providing 500 sampling points per sinusoid and ~20 sampling points between two successive maxima of the interference signal for this current amplitude, which is well above the Nyquist limit.

The amplitude of the frequency modulation, $\Delta\nu$, and its phase, ϕ_{FM} is obtained by fitting the peaks in the resonator trace, translated to a frequency scale through the FSR, to an equation of the form

$$y = C + \Delta\nu\cos(\omega t + \phi_{FM}) \tag{10}$$

where C is a DC offset defined by the allocation of the first resonator peak at a frequency value of zero.

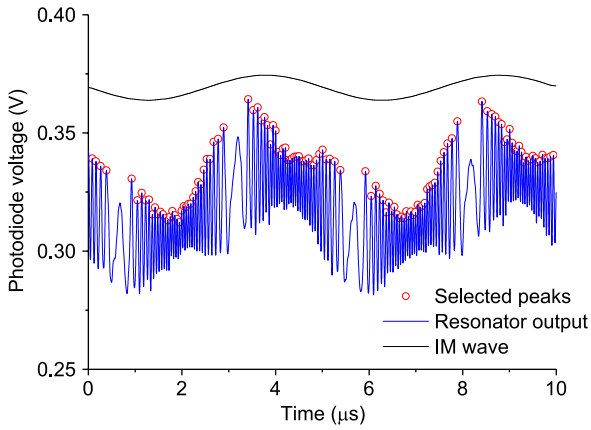

Fig. 2. Fiber resonator response with laser current modulation.

The output of the measurement arm provides the intensity output of the laser, which can be fit to an equation of the form

$$y = I + \Delta I \cos(\omega t + \phi_{IM}) + \Delta I_2 \cos(2\omega t + \phi_{2IM}) \tag{11}$$

where I is the DC intensity of the laser, ΔI and ΔI_2 are the linear and non-linear IM amplitudes, and ϕ_{IM} and ϕ_{IM2} are their phases with respect to the current modulation.

The WM phase lag with respect to the current modulation is then given as

$$\psi_\lambda = \phi_{IM} - \phi_{FM} + \pi \tag{12}$$

and the tuning coefficient is calculated as $\Delta\nu/\Delta i$ (GHz/mA), where Δi is the applied current modulation amplitude (mA). Allowance is made for the phase delay of 0.09° caused by the difference in path-length between the wavelength referencing arm and the measurement arm.

4.2. Experimental Frequency Response

The measured magnitude of the tuning coefficient of the DFB-MQW laser as a function of modulation frequency is shown in Fig. 3. For measurements below 100 kHz the bias-T (see Fig. 1) is removed and a summing amplifier is used prior to the current controller, which has a low-pass cut-off frequency of 250 kHz.

Compared with DFB lasers used in the optical communications band, the tuning coefficient presents some unusual features. Intuitively, we might expect the tuning coefficient to monotonically decrease with modulation frequency as the thermal contribution reduces. However, we note from the high frequency region of the tuning characteristic in Fig. 3, where the thermal contribution becomes small, that the carrier contribution has a relatively large magnitude of ~0.27 GHz/mA. Hence, the condition that $2\rho_f > H_0$, as discussed in relation to the simple RC model of equation (1), is satisfied which predicts an increasing tuning coefficient with modulation frequency. There is also an initial dip in the response which cannot be explained on the basis of the simple RC thermal model. This type of behavior is predicted by the more advanced thermal model of equation (5) where the thermal WM lag increases more slowly with frequency rather than approaching 90°. However it should be noted that the thermal model outlined in the Appendix is based on a simplified planar model and predicts the general trends rather than giving an exact match to the experimental results.

The measured WM-IM phase lag is shown in Fig. 4 for different bias currents. It can be observed from Fig. 4 that the phase shift approaches 180° as the thermal effect diminishes at high frequencies. The phase shift is also bias current dependent. As discussed in Section 2,

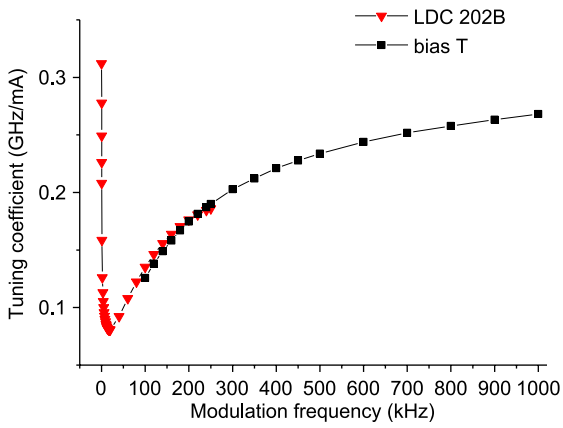

Fig. 3. Tuning coefficient as a function of the modulation frequency for a constant bias current of 70 mA.

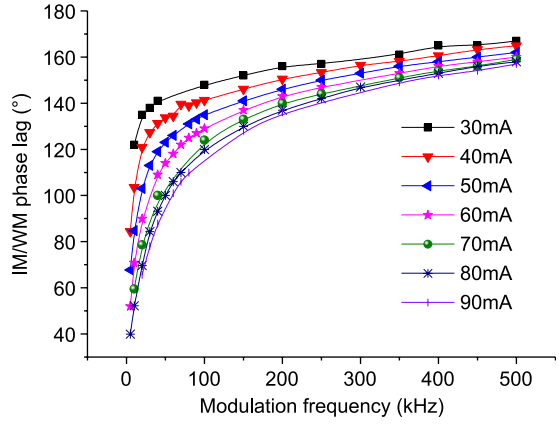

Fig. 4. Variation in WM-IM phase lag as a function of modulation frequency for varying dc bias currents.

this may be explained as a result of the increased thermal effect at higher bias currents from ohmic heating, reducing the overall phase shift when combined with the carrier effect.

The effect of bias current on the phase shift at a modulation frequency of 100 kHz is shown in Fig. 5 for various TEC temperatures. This phase shift as a function of bias current has a significant effect on the recovered signals in the PDM. For a given bias current, the phase shift increases with temperature, suggesting a reduced thermal modulation effect at higher TEC temperatures. This may result from increased heat loss by radiation from the laser diode or from a reduced thermal resistance at higher temperatures.

5. Correction for Modulation Effects

In this section, we illustrate the use of the PDM for line shape recovery, for the case of CO_2 detection with the DFB- MQW laser described in Section 4. The measurement arrangement is the same as shown in Fig. 1, with a calibrated mixture of CO_2 and nitrogen used instead of pure nitrogen. A 5 Hz saw-tooth current ramp and a sinusoidal modulation were applied to the laser using the bias-T configuration. The detected gas absorption signal is demodulated using an

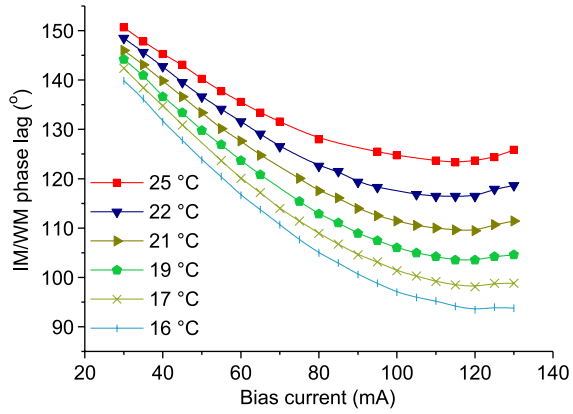

Fig. 5. Measured WM-IM phase lag as a function of bias current at different TEC temperatures.

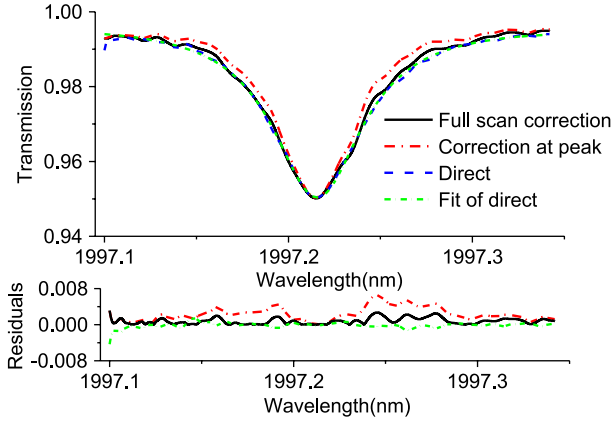

Fig. 6. Effect of phase walk-off for a single CO_2 absorption line. C = 100%, T = 22 °C, P = 1.013 bar, and m = 0.08.

SR-830 digital lock in amplifier, whose X and Y output channels were displayed on a Tektronix oscilloscope (TDS 3014 B) and recorded via a GPIB interface.

The variations in the WM-IM phase, shown Fig. 5, need to be considered to ensure accurate recovery of line shapes using the PDM. In this section we show the effect of using a single value of the WM-IM phase using the PDM and how we can use phase walk-off correction to obtain accurate line shapes from the PDM with measurements independent of the lock-in phase.

The effect of phase walk-off on the recovered line shape of a single CO_2 absorption line at 1997.22 nm with PDM is shown in Fig. 6, for a path length of 6 cm, a temperature of 21 °C and a concentration of 100%. Here, the direct line shape profile is compared with the case where ψ_λ has a fixed value, calculated at line center, and where ψ_λ is adjusted with current according to Fig. 5. The modulation frequency is 200 kHz and modulation index is 0.084. The variation in the magnitude of *m* across the scan was measured as ~5% but has a negligible effect on the line shape recovery. As shown, taking into account the phase walk-off provides more accurate recovery of the absorption profile, particularly the width of the line shape. A least-square fitting algorithm was used to obtain concentration and temperature values by comparing the corrected and uncorrected PDM signals to a theoretical model.

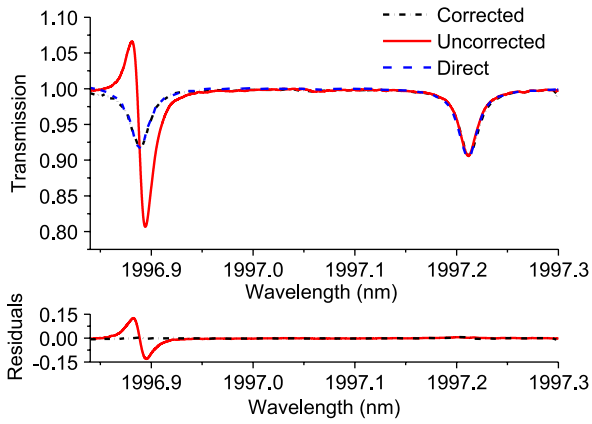

Fig. 7. Effect of phase walk-off on line shape recovery for a scan across two CO_2 lines. The incomplete cancellation of the 1-f signal is apparent at shorter wavelengths.

Concentration and temperature measurements of $C = 102\%$ and $T = 21.35\ ^{\circ}C$ for the corrected signal and $C = 67.8\%$ and $T = 67.4\ ^{\circ}C$ for the uncorrected signal were calculated, highlighting the importance of taking into account the modulation phase characteristics of any optical source used in TDLS-WMS applications.

The effect is even more dramatic in Fig. 7 which shows the experimentally recovered line shape of two CO_2 features, as would be necessary for ratio thermometry using a single laser source. The PDM with and without phase correction is used at a modulation frequency of 50 kHz and the modulation index of $m \sim 0.2$. The direct signal, obtained under the same conditions is also shown as a comparison. Where correction is applied the phase shift across the scan is determined from the phase response as in Fig. 5 and the correct phase value is applied to each λ-point in the PDM computation, as described in equation (6). Again, for low m-values, changes in the magnitude of m across the scan have a negligible effect on the measured signals. The results in Fig. 7 clearly indicate the need for phase correction and demonstrate that accurate line shape recovery can be achieved through the PDM technique. As ratio thermometry uses the ratio of the peak absorbance of the two features, it is clear that the phase correction is essential if accurate temperature data is to be acquired using the PDM.

For the PDM data shown in Fig. 7, the orientation of the lock-in amplifier x-axis was aligned with the RAM component. This is achieved by ensuring the y-axis output is on a zero background. In the case of significant phase walk-off the RAM component is never fully isolated on the x-axis, and a projection of the RAM will be present on the y-axis output over the majority of the current scan, thus making alignment impossible.

Use of the analytical procedure described in Section 3.2, where the orientation of the lock-in axes does not require pre-alignment, therefore simplifies the measurement procedure. Fig. 8 shows the results obtained for two different orientations of the axes with phase correction applied, further verifying the advantage of this technique.

6. Conclusion

A wide variety of laser types are used for WMS and in this work we have reviewed the basic modulation properties of DFB lasers to identify some of the key issues that affect the design and operation of WMS systems. Important features highlighted include the phase walk-off from joule heating and the effect of the carrier contribution on whether the magnitude of the frequency response decreases or increases with modulation frequency. These are important considerations in the choice of modulation frequency. For example, a higher modulation frequency reduces the phase walk-off and may in some cases give a larger wavelength modulation. The physical dimensions of the laser chip are also important in determining the thermal resistance and hence

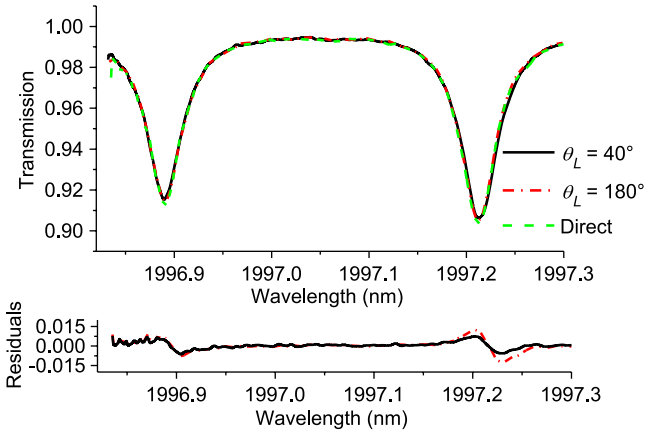

Fig. 8. Axes invariant results corrected for phase-walk.

the magnitude of the thermal contribution. The PDM approach has been improved by removing the need to pre-set the orientation of the lock-in axes and we have demonstrated how this approach may be used to correct signals for phase walk-off for the particular case of CO_2 detection with a quantum well laser. Other lasers will exhibit similar features to a greater or lesser extent, depending on the laser type and the magnitude of the current scan, and knowledge of the basic laser parameters along with the simple models outlined in the paper can assist in optimizing the operation of WMS systems.

Appendix
Thermal Wavelength Modulation

We first consider a simple 1-D analytical model [29], [30] based on the laser chip having a thermal capacity C_T and a thermal resistance R_T to the heat sink which conducts all the heat energy away from the chip. This leads to the simple thermal equation for the laser diode temperature T as

$$C_T \frac{dT}{dt} + \frac{T - T_0}{R_T} = P_{el} \tag{A.1}$$

where P_{el} is the electrical power dissipated in the chip, and T_0 is the heat sink temperature.

For WMS applications, the forward injection current, i_f, supplied to the DFB laser takes the form: $i_f = I_{\text{bias}} + i_m \cos(\omega_m t)$ where I_{bias} is the DC bias current, i_m is the modulation current amplitude, and ω_m is the modulation frequency. The forward diode voltage is approximated by $v_f \cong V_j + i_f r_s$ so the electrical power dissipated in the chip is

$$P_{el} = v_f i_f - P_{opt} = [V_j i_f - P_{opt}] + i_f^2 r_s \tag{A.2}$$

where r_s the series resistance of the laser chip (obtained from the slope of the VI characteristic), V_j is the junction voltage, and P_{opt} is the output optical power given by $P_{opt} = \eta \cdot (I_{\text{bias}} - I_{th})$ where I_{th} is the threshold current and η is the slope efficiency (slope of the optical power versus current characteristic). We assume the laser is above threshold and the spontaneous emission power is neglected.

The DC and AC heat generated follows from (A.2)

$$P_{\text{el}} = P_{\text{DC}} + A_1 \cos(\omega_m t) + A_2 \cos(2\omega_m t) \tag{A.3}$$

where P_{DC}, A_1, and A_2 are given by

$$P_{\mathrm{DC}} = \left[V_j I_{\mathrm{bias}} - \eta \cdot (I_{\mathrm{bias}} - I_{th})\right] + \left[r_s I_{\mathrm{bias}}^2 + \frac{r_s i_m^2}{2}\right] \tag{A.4}$$

$$A_1 = (V_j - \eta) \cdot i_m + 2 r_s I_{\mathrm{bias}} i_m \tag{A.5}$$

$$A_2 = \frac{r_s i_m^2}{2}. \tag{A.6}$$

Substitution of the electrical power from (A.3) into (A.1) and neglecting A_2 gives the temperature change

$$T = T_0 + R_T \left\{ P_{\mathrm{DC}} + \frac{A_1 \cos(\omega_m t - \varphi_1)}{\sqrt{1 + \omega_m^2 \tau_{th}^2}} \right\} \tag{A.7}$$

where τ_{th} is the thermal time constant given by $\tau_{th} = R_T C_T$ and the thermal phase lag $\varphi_1 = tan^{-1}(\omega_m \tau_{th})$.

The change in the laser's output wavelength is related to the change in temperature by the temperature tuning coefficient $\Delta\lambda/\Delta T$ so that the thermal DC tuning and wavelength modulation are given by

$$\lambda = \lambda_0 + \left(\frac{\Delta\lambda}{\Delta T}\right) R_T \left\{ P_{\mathrm{DC}} + \frac{A_1 \cos(\omega_m t - \varphi_1)}{\sqrt{1 + \omega_m^2 \tau_{th}^2}} \right\} \tag{A.8}$$

where $\Delta\lambda/\Delta T = (\alpha_I + \alpha_n)\lambda$, and α_I and α_n are thermal linear expansion and refractive index coefficients, respectively. Typically, $\Delta\lambda/\Delta T \approx 0.11$ nm/°C. The thermal resistance, R_T, for one-dimensional heat flow from the active layer to the heat sink is given by, $R_T = d_s/kA$, where d_s is the thickness of the substrate (distance of the active layer from the heat sink), A is the area of the active layer and k is the thermal conductivity (~ 0.68 W/cm °K for InP at 300 °K). More realistically, the quasi two-dimensional heat flow from an active layer of width w and length l to a heat sink at a distance d_s gives a thermal resistance of [29]

$$R_T = \frac{ln\left(\frac{4d_s}{w}\right)}{\pi k l} \tag{A.9}$$

with typical values of $R_T \approx 30 - 50$ °C/W.

To improve on the RC model, we derive below a simple 1-D analytical solution (which reduces to (A.8) at low frequencies) from the heat conduction equation for the temperature of the active layer. We consider the 1-D planar structure shown in Fig. A1 where we assume uniform heat generation from electrical power dissipation $P_{el}(t)$ in the thin active layer of thickness d_a, positioned at a distance d_s from the heat sink, with a top buffer or confinement layer of thickness d_b.

The heat generated in the active layer from equation (A.3) is written in exponential notation as

$$P_{\mathrm{el}}(t) \approx P_{\mathrm{DC}} + A_1 e^{j\omega_m t}. \tag{A.10}$$

We assume that the temperature throughout the thin active layer (and over the optical profile) is approximately uniform if $d_a \ll d_s$ and is given by $T_{ss} + T_a(t)$, where

$$T_a(t) = T_a e^{j(\omega_m t + \varphi)} \tag{A.11}$$

$$T_{\mathrm{ss}} = R_T P_{\mathrm{DC}} + T_0 \tag{A.12}$$

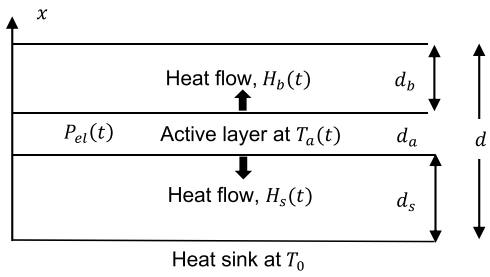

Fig. A1. Heat flow in simplified planar laser structure.

T_{ss} is the steady-state temperature of the active region, T_0 is the heat sink temperature, and R_T is the thermal resistance to the heat sink.

For boundary conditions, we assume a fixed temperature of T_0 at $x = 0$ (heat sink), and we further assume that there is no heat loss from the upper surface so that $\partial T/\partial x = 0$ at $x = d$. The heat flow out of the active layer, with thermal capacity C_a, is represented by $H_s(t)$ and $H_b(t)$.

For the upper and lower regions where we assume that no heat generation occurs, the heat conduction equation has the form

$$\frac{dT}{dt} = \kappa \frac{d^2T}{dx^2} \tag{A.13}$$

which has the following time-varying solutions:

$$T(x,t) = T_a(t)\left[\frac{e^{qx} - e^{-qx}}{e^{qd_s} - e^{-qd_s}}\right],\ 0 \le x \le d_s \tag{A.14}$$

$$T(x,t) = T_a(t)\left[\frac{e^{q(x-d)} + e^{-q(x-d)}}{e^{qd_b} + e^{-qd_b}}\right],\ (d_s + d_a) \le x \le d \tag{A.15}$$

where $q = \sqrt{j\omega_m/\kappa}$, $\kappa = k/(\rho C_p)$ is the thermal diffusivity, ρ is the density, and C_p is the specific heat capacity (typically, $\rho \sim 4.81$ g/cm^3, $C_p \sim 0.31$ J/g $^\circ\kappa$, and $\kappa \sim 0.46$ cm^2/s for InP at 300 $^\circ\kappa$).

Since heat flow is given by: $H = -kA(\partial T/\partial x)$, it follows from (A.14) and (A.15) that the heat flow out of the active layer is given by

$$H_s(t) = kAqT_a(t)\coth(qd_s) \tag{A.16}$$

$$H_b(t) = kAqT_a(t)\tanh(qd_b). \tag{A.17}$$

Note that when $qd_s \ll 1$ (A.14) reduces to a linear temperature distribution and (A.16) becomes: $H_s(t) \approx T_a(t)(1 + (1/2)j\omega_m R_T C_s)/\mathrm{R}_T$. Similarly, for $qd_b \ll 1$, (A.17) becomes: $H_b(t) \approx j\omega_m C_b T_a(t)$, consistent with the simple RC thermal model. C_b and C_s are the thermal capacitances of the top and substrate layers, respectively, given by $C = \rho C_p V$ and the thermal resistance, $R_T = d_s/kA$.

Energy balance in the active layer requires that

$$C_a \frac{dT_a(t)}{dt} + H_s(t) + H_b(t) = P_{el}(t) \tag{A.18}$$

where C_a is the thermal capacity of the active layer.

Combining equations (A.10), (A.11), (A.16), (A.17) with (A.18), we obtain

$$T_a(t) = \frac{A_1 e^{j\omega_m t}}{j\omega_m C_a + kAq\left[\coth(qd_s) + \tanh(qd_{b)}\right]}. \tag{A.19}$$

From (A.11), (A.12), and (A.19), the active layer temperature is

$$T = T_0 + R_T\left\{P_{\mathrm{DC}} + \frac{A_1 e^{j\omega_m t}}{j\omega_m R_T C_a + qd_s\left[\coth(qd_s) + \tanh(qd_{b)}\right]}\right\}. \tag{A.20}$$

Note that, for qd_s and $qd_b \ll 1$, (A.20) reduces to the simple RC thermal model

$$T = T_0 + R_T\left\{P_{\mathrm{DC}} + \frac{A_1 e^{j\omega_m t}}{1 + j\omega_m R_T C_T}\right\} \tag{A.21}$$

with $C_T = C_a + C_b + (1/2)C_s$.

If we define cut-off frequencies associated with the substrate, top and active layers by $\omega_{cs} = \kappa/d_s^2$, $\omega_{cb} = \kappa/d_b^2$ and $\omega_{ca} = (d_s/d_a)\omega_{cs}$, then (A.20) becomes

$$T = T_0 + R_T\left\{P_{\mathrm{DC}} + \frac{A_1 e^{j\omega_m t}}{j\omega_m/\omega_{ca} + \left(\frac{j\omega_m}{\omega_{cs}}\right)^{\frac{1}{2}}\left[\coth\left(\frac{j\omega_m}{\omega_{cs}}\right)^{\frac{1}{2}} + \tanh\left(\frac{j\omega_m}{\omega_{cb}}\right)^{\frac{1}{2}}\right]}\right\}. \tag{A.22}$$

The thermal DC tuning and wavelength modulation is then

$$\lambda = \lambda_0 + \left(\frac{\Delta\lambda}{\Delta T}\right)R_T\left\{P_{\mathrm{DC}} + \frac{A_1 e^{j\omega_m t}}{j\omega_m/\omega_{ca} + \left(\frac{j\omega_m}{\omega_{cs}}\right)^{\frac{1}{2}}\left[\coth\left(\frac{j\omega_m}{\omega_{cs}}\right)^{\frac{1}{2}} + \tanh\left(\frac{j\omega_m}{\omega_{cb}}\right)^{\frac{1}{2}}\right]}\right\}. \tag{A.23}$$

Typically, d_s is around three orders of magnitude greater than d_a so that $\omega_{ca} \gg \omega_{cs}$ and the first term in the denominator may be neglected for sub-megahertz modulation frequencies.

Acknowledgment

This work was done as part of the Fiber Laser Imaging of gas Turbine Exhaust Species (FLITES) project and an EPSRC grant.

References

[1] J. T. C. Liu *et al.*, "Near-infrared diode laser absorption diagnostic for temperature and water vapor in a scramjet combustor," *Appl. Opt.*, vol. 44, no. 31, pp. 6701–6711, Nov. 2005.
[2] H. Li, G. B. Rieker, X. Liu, J. B. Jeffries, and R. K. Hanson, "Extension of wavelength-modulation spectroscopy to large modulation depth for diode laser absorption measurements in high-pressure gases," *Appl. Opt.*, vol. 45, no. 5, pp. 1052–1061, Feb. 2006.
[3] W. Johnstone, A. J. McGettrick, K. Duffin, A. Cheung, and G. Stewart, "Tunable diode laser spectroscopy for industrial process applications: system characterization in conventional and new approaches," *IEEE Sens. J.*, vol. 8, no. 7, pp. 1079–1088, Jul. 2008.
[4] A. J. McGettrick, W. Johnstone, R. Cunningham, and J. D. Black, "Tunable diode laser spectroscopy with wavelength modulation: calibration free measurements of gas compositions at elevated temperatures and varying pressure," *J. Lightw. Technol.*, vol. 27, no. 15, pp. 3150–3161, Aug. 2009.
[5] G. B. Rieker, J. B. Jeffries, and R. K. Hanson, "Calibration-free wavelength-modulation spectroscopy for measurements of gas temperature and concentration in harsh environments," *Appl. Opt.*, vol. 48, no. 29, pp. 5546–5560, Oct. 2009.
[6] K. Sun *et al.*, "Analysis of calibration-free wavelength-scanned wavelength modulation spectroscopy for practical gas sensing using tunable diode lasers," *Meas. Sci. Technol.*, vol. 24, no. 12, Oct. 2013, Art. no. 125203.

[7] C. S. Goldenstein *et al.*, "Fitting of calibration-free scanned-wavelength-modulation spectroscopy spectra for determination of gas properties and absorption lineshapes," *Appl. Opt.*, vol. 53, no. 3, pp. 356–67, Jan. 2014.
[8] P. Wright *et al.*, "Progress towards non-intrusive optical measurement of gas turbine exhaust species distributions," in *Proc. IEEE Aerosp. Conf.*, 7–14, Mar. 2015, pp. 1–14. [Online]. Available: doi:10.1109/AERO.2015.7119019
[9] T. Fernholz, H. Teichert, and V. Ebert, "Digital, phase-sensitive detection for in situ diode-laser spectroscopy under rapidly changing transmission conditions," *Appl. Phys. B*, vol. 75, no. 2–3, pp. 229–236, Sep. 2002.
[10] J. A. Silver, "Frequency-modulation spectroscopy for trace species detection: Theory and comparison among experimental methods," *Appl. Opt.*, vol. 31, no. 6, pp. 707–717, 20, Feb. 1992.
[11] J. M. Supplee, E. A. Whittaker, and W. Lenth, "Theoretical description of frequency modulation and wavelength modulation spectroscopy," *Appl. Opt.*, vol. 33, no. 27, pp. 6294–6302, Sep. 1994.
[12] P. Kluczynski and O. Axner, "Theoretical description based on Fourier analysis of wavelength—Modulation spectrometry in terms of analytical and background signals," *Appl. Opt.*, vol. 38, no. 27, pp. 5803–5815, Sep. 1999.
[13] P. Kluczynski, A. M. Lindberg, and O. Axner, "Characterization of background signals in wavelength—Modulation spectrometry in terms of a Fourier based formalism," *Appl. Opt.*, vol. 40, no. 6, pp. 770–782, Feb. 2001.
[14] P. Kluczynski, A. M. Lindberg, and O. Axner, "Background signals in wavelength modulation spectrometry with frequency—Doubled diode-laser light. I. Theory," *Appl. Opt.*, vol. 40, no. 6, pp. 783–793, Feb. 2001.
[15] S. Schilt, L. Thevenaz, and P. Robert, "Wavelength modulation spectroscopy: Combined frequency and intensity laser modulation," *Appl. Opt.*, vol. 42, no. 33, pp. 6728–6738, Nov. 2003.
[16] V. G. Avetisov and P. Kauranen, "High-resolution absorption measurements by use of two-tone frequency-modulation spectroscopy with diode lasers," *Appl. Opt.*, vol. 36, no. 18, pp. 4043–4054, Jun. 1997.
[17] K. Duffin, A. J. McGettrick, W. Johnstone, G. Stewart, and D. G. Moodie, "Tunable diode-laser spectroscopy with wavelength modulation: A calibration-free approach to the recovery of absolute gas absorption line shapes," *J. Lightw. Technol.*, vol. 25, no. 10, pp. 3114–3125, Oct. 2007.
[18] A. J. McGettrick, K. Duffin, W. Johnstone, G. Stewart, and D. G. Moodie, "Tuneable diode laser spectroscopy with wavelength modulation: A phasor decomposition method for calibration free measurements of gas concentration and pressure," *J. Lightw. Technol.*, vol. 26, no. 4, pp. 432–440, Feb. 2008.
[19] K. Ruxton *et al.*, "Tunable diode laser spectroscopy with wavelength modulation: Elimination of residual amplitude modulation in a phasor decomposition approach," *Sens. Actuators, B, Chem.*, vol. 150, no. 1, pp. 367–375, Sep. 2010.
[20] G. Stewart, W. Johnstone, J. R. P. Bain, K. Ruxton, and K. Duffin, "Recovery of absolute gas absorption line shapes using tunable diode laser spectroscopy with wavelength modulation—Part I: Theoretical analysis," *J. Lightw. Technol.*, vol. 29, no. 6, pp. 811–821, 2011.
[21] J. R. P. Bain *et al.*, "Recovery of absolute gas absorption line shapes using tunable diode laser spectroscopy with wavelength modulation—Part II: Experimental investigation," *J. Lightw. Technol.*, vol. 29, no. 7, pp. 987–996, 2011.
[22] R. S. Tucker, "High-speed modulation of semiconductor lasers," *J. Lightw. Technol.*, vol. LT-3, no. 6, pp. 1180–1192, Dec. 1985.
[23] O. Doyle, P. B. Gallion, and G. Debarge, "Influence of carrier nonuniformity on the phase relationship between frequency and intensity modulation in semiconductor lasers," *IEEE J. Quant. Electron.,*, vol. 24, no. 3, pp. 516–522, Mar. 1988.
[24] S. Schilt and L. Thevenaz, "Experimental method based on wavelength-modulation spectroscopy for the characterization of semiconductor lasers under direct modulation," *Appl. Opt.*, vol. 43, no. 22, pp. 4446–4453, 1, Aug. 2004.
[25] A. Hangauer, J. Chen, R. Strzoda, and M. C. Amann, "The frequency modulation response of vertical-cavity surface-emitting lasers: Experiment and theory," *IEEE J. Sel. Top. Quant. Electron.*, vol. 17, no. 6, pp. 1584–1593, Nov./Dec. 2011.
[26] J. Li, Z. Du, and Y. An, "Frequency modulation characteristics for interband cascade lasers emitting at 3 μm," *Appl. Phys. B*, vol. 121, no. 1, pp. 7–17, Oct. 2015.
[27] S. Kobayashi, Y. Yamamoto, M. Ito, and T. Kimura, "Direct frequency modulation in AlGaAs semiconductor lasers," *IEEE J. Quant. Electron.*, vol. QE-18, no. 4, pp. 582–595, Apr. 1982.
[28] G. Morthier and P. Vankwikelberge, *Handbook of Distributed Feedback Laser Diodes*, 2nd ed. Norwood, MA, USA: Artech House, 2013.
[29] L. A. Coldren and S. W. Corzine, *Diode Lasers and Photonic Integrated Circuits*. New York, NY, USA: Wiley, 1995, p. 56.
[30] Y. Yamamoto, *Coherence, Amplification and Quantum Effects in Semiconductor Lasers*. New York, NY, USA: Wiley, pp 122–126, 1991.
[31] P. Vankwikelberge *et al.*, "Analysis of the carrier-induced FM response of DFB lasers: Theoretical and experimental case studies," *IEEE J. Quant. Electron.*, vol. 25, no. 11, pp. 2239–2254, Nov. 1989.
[32] R. Schatz, "Dynamics of spatial hole burning effects in DFB lasers," *IEEE J. Quant. Electron.*, vol. 31, no. 11, pp. 1981–1993, Nov. 1995.
[33] J. Kinoshita, "Modelling of high-speed DFB lasers considering the spatial holeburning effect using three rate equations," *IEEE J. Quant. Electron.*, vol. 30, no. 4, pp. 929–938, Apr. 1994.
[34] J. Kinoshita and K. Matsumoto, "Transient chirping in distributed feedback lasers: Effect of spatial hole-burning along the laser axis," *J. Quant. Electron.*, vol. 24, no. 11, pp. 2160–2169, Nov. 1988.
[35] H. S. Carslaw and J. C. Jaeger, *Conduction of Heat in Solids*. London, U.K.: Oxford Univ. Press, 1959.
[36] W. B. Joyce and R. W. Dixon, "Thermal resistance of heterostructure lasers," *J. Appl. Phys.*, vol. 46, no. 2, pp. 855–862, Feb. 1975.
[37] M. Ito and T. Kimura, "Stationary and transient thermal properties of semiconductor laser diodes," *IEEE J. Quant. Electron.*, vol. QE-17, no. 5, pp. 787–795, May 1981.
[38] G. S. Pandian and S. Dilwali, "On the thermal response of a semiconductor laser diode," *IEEE Photon. Technol. Lett.*, vol. 4, no. 2, pp. 130–133, Feb. 1992.
[39] P. Correc, O. Girard, and I. F. de Faria, "On the thermal contribution to the FM response of DFB lasers: Theory and experiment," *IEEE J. Quant. Electron.*, vol. 30, no. 11, pp. 2485–2490, Nov. 1994.

[40] S. Dilwali and G. Soundra Pandian, "Transfer function of thermal FM, FSK step response and the dip in the FM response of laser diodes," *Opt. Quant. Electron.*, vol. 24, no. 6, pp. 661–676, Jun. 1992.
[41] M. Funabashi *et al.*, "Recent advances in DFB lasers for ultradense WDM applications," *IEEE J. Sel. Top. Quant. Electron.*, vol. 10., no. 2, pp. 312–320, Mar./Apr. 2004.
[42] X. Li and W.-P. Huang, "Simulation of DFB semiconductor lasers incorporating thermal effects," *IEEE J. Quant. Electron.*, vol. 31, no. 10, pp. 1848–1855, Oct. 1995.
[43] J. Buus, M. C. Amman, and D. J. Blumenthal, *Tunable Laser Diodes and Related Optical Sources*. Hoboken, NJ, USA: Wiley, 2005, pp. 102–104.
[44] A. L. Chakraborty, K. Ruxton, W. Johnstone, M. Lengden, and K. Duffin, "Elimination of residual amplitude modulation in tunable diode laser wavelength modulation spectroscopy using an optical fiber delay line," *Opt. Exp.*, vol. 17, no. 12, pp. 9602–9607, Jun. 2009. [Online]. Available: doi:10.1364/OE.17.009602
[45] J. R. P. Bain, M. Lengden, G. Stewart, and W. Johnstone, "Recovery of absolute absorption line shapes in tunable diode laser spectroscopy using external amplitude modulation with balanced detection," *IEEE Sens. J.*, vol. 16, no. 3, pp. 675–680, Feb. 2016.
[46] R. Phelan *et al.*, "$In_{0.75}Ga_{0.25}As$/ InP multiple quantum-well discrete-mode laser diode emitting at 2 μm," *IEEE Photon. Technol. Lett.*, vol. 24, no. 8, pp. 652–654, Apr. 2012.